Fully Simulated Data-Driven Domain Generalized Method for Multiphase Converters Fault Diagnosis

Haoxiang Xu, *Student Member, IEEE*, Zicheng Liu, *Senior Member, IEEE*, Guangyu Wang, *Student Member, IEEE*, Dong Jiang, *Senior Member, IEEE*, and Wei Sun, *Member, IEEE*

***Abstract*—This article investigates the generalization capabilities of deep learning models for diagnosing faults in multiphase converter power switch devices. Traditional fault diagnosis approaches depend heavily on real-world fault data for model training. However, in industrial settings, the infrequent failures of multiphase converters and the prohibitive costs of fault experiments result in a significant scarcity of actual fault data. This limitation diminishes the reliability of models trained solely on simulation data when applied to real-world situations. To overcome this challenge, this article proposes an innovative method to improve cross-domain fault diagnosis efficacy without relying on experimental domain samples. Initially, the research employs a normalization preprocessing strategy that utilizes phase current reconstruction to minimize temporal disparities among samples. A convolutional autoencoder is then used to extract deep features from the multiphase current signals. Additionally, this article integrates deep metric learning with classification techniques to enhance the model's discrimination and clustering abilities. The key advantage of this method is that in scenarios where experimental domain data is scarce, the generalization diagnosis of open-circuit faults in multiphase motor drive systems with various parameters and types can be achieved using only simulation domain data. Furthermore, robustness and rapid fault diagnosis are realized. Experimental results and comparative analyses prove the effectiveness of the developed diagnostic algorithm. Moreover, we have made all the datasets used in this article publicly available.**

***Index Terms*—Deep metric learning, domain generalization, fault diagnosis, normalization preprocessing.**

I. Introduction

COMPARED to traditional three-phase motors, multiphase motors offer significant enhancements in power density due to the increased number of phases. They also effectively reduce torque ripple and motor noise, while providing superior fault-tolerance performance [1]. Nevertheless, a greater number of phases introduces challenges, primarily an increase in component count, which elevates the potential for failures. During operation, power devices can suffer damage from overvoltage, overcurrent, and aging. Additionally, extreme conditions such as high temperatures and vibrations may lead to solder detachment, resulting in an open-circuit fault (OCF) [2]. Unlike short-circuit faults, which display conspicuous symptoms such as overcurrent or high temperatures, OCF have subtle manifestations that often fail to activate hardware protections, thus delaying detection and potentially causing subsequent faults. Consequently, there is an increasing need to diagnose OCF in power devices within multiphase motor systems. This diagnosis provides essential information for fault-tolerant control and enhances system reliability [3].

Fault diagnosis methods are broadly classified into model-based, signal-based, and data-driven approaches [4]. Model-based methods utilize physical principles or system identification techniques to construct models of the system. These methods compute and monitor discrepancies between the outputs generated by the model and the actual measured outputs, facilitating the detection and localization of anomalies and faults. Examples of these techniques include observer methods [5] and state estimation methods [6]. However, the effectiveness of model-based approaches is contingent upon the accuracy of the mathematical models, which can lead to challenges related to model uncertainty and parameter identification. In contrast, signal-based methods are especially prevalent in systems that are difficult to model. These methods diagnose the health of the system by identifying fault characteristic components within sampled signals, such as voltage signals [7] and current signals [8]. Since signal-based methods rely on advanced signal processing technologies and predetermined hyperparameter settings, they can impose significant computational demands and require extensive tuning periods.

With the rapid advancement of artificial intelligence technology, the application of machine learning in fault diagnosis has emerged as a significant research focus within the fields of science and engineering [9]. This methodology primarily involves establishing a mapping relationship between measured data and corresponding fault labels. During the offline training phase, fault databases are utilized to develop diagnostic models using machine learning techniques. Subsequently, in the online application phase, these models generate diagnostic outcomes based on the input signals. This data-driven approach reduces dependency on system modeling and signal processing, thereby

Received 21 May 2024; revised 2 August 2024; accepted 9 September 2024. Date of publication 13 September 2024; date of current version 12 December 2024. This work was supported in part by the National Natural Science Foundation of China (NSFC) under Grant 52077088, and in part by the Aeronautical Science Foundation of China under Grant 2022Z027079001. Recommended for publication by Associate Editor A. Marques Cardoso. *(Corresponding author: Zicheng Liu.)*

The authors are with the School of Electrical and Electronic Engineering, Huazhong University of Science and Technology, Wuhan 430074, China (e-mail: haoxiangxu@hust.edu.cn; liuzc@hust.edu.cn; guangyuwang@hust.edu.cn; jiangd@hust.edu.cn; sunwei77@hust.edu.cn).

The database can be accessed at https://github.com/XHX-HUST/Multiphase-converter-switching-device-open-circuit-fault-data-set.git.

Color versions of one or more figures in this article are available at https://doi.org/10.1109/TPEL.2024.3461159.

Digital Object Identifier 10.1109/TPEL.2024.3461159

enhancing robustness and universality in nonlinear time-varying systems. Hang et al. [10] have improved the noise resistance of models and achieved precise identification of 22 types of faults in power switching devices under diverse operating conditions. They accomplished this by integrating normalized current vector trajectory graphs with wavelet convolutional neural networks to process stator phase currents in permanent magnet synchronous motor (PMSM). Zhang et al. [11] utilized three-phase current and bus voltage signals to develop a fault diagnosis model using an improved particle swarm optimization (PSO) and support vector machine (SVM) algorithm, aimed at enhancing robustness and accuracy. In [12], critical features were initially selected using the fast Fourier transform (FFT) and the ReliefF feature selection algorithm. Following this, a random vector functional link network was trained to diagnose faults in IGBT and current sensors. Diagnostic variables were chosen based on an explicit analytical model of converters, while the self-learning capabilities of artificial neural networks were leveraged to navigate the complexities of fault analysis, rule setting, and threshold determination [13]. Although the effectiveness of these models has been demonstrated, they still depend heavily on extensive training with large datasets of real fault data.

In recent years, numerical simulation has emerged as a powerful tool for addressing data scarcity in fault diagnosis [14]. Previous studies have suggested enhancing datasets through the integration of simulation tools for systems such as the ac–dc–ac electrical railway traction [15] and subsea electric actuator PMSM drives [16], where comprehensive fault states and data samples under varied load conditions are often unattainable through experimental measures. However, these studies presuppose the availability of a limited set of labeled or unlabeled data from the experimental domain, leveraging the supervised self-correction of network models to bridge domain discrepancies. This approach enables models to train on extensive simulation domain fault data and achieve effective generalization in experimental domain classification tasks. Such domain adaptation strategies have significantly advanced the evolution of data-driven methodologies. Despite their improved efficacy in managing cross-domain diagnostic challenges compared to previous methods, these strategies exhibit inherent limitations [17]. Specifically, fault data from the experimental domain, whether it consists of a small number of labeled samples or a larger set of unlabeled samples, is essential for facilitating positive knowledge transfer to the simulation domain. However, collecting experimental fault data from the targeted system often entails significant costs and high security risks, particularly in fields such as wind power generation, aerospace, and traction systems [18], [19], [20]. Consequently, in real industrial environments, it is typically impractical to rely on historical data or on-site experiments to preliminarily obtain fault data specific to the target motor system. Furthermore, the idealized assumptions used in numerical simulations, coupled with the neglect of various uncertain factors in real-world applications, often result in models trained exclusively on simulation databases being unable to effectively extract complex features from experimental data. This limitation can lead to high rates of fault misdiagnosis [21]. Thus, a key challenge in the field of fault diagnosis remains determining how to theoretically bridge the gap between simulated and experimental data. Ensuring that models trained solely on simulated data continue to exhibit superior diagnostic capabilities when confronted with unpredictable experimental data is critical. Addressing this significant impediment that the scarcity of real-world fault data presents to the practical application of intelligent diagnostic algorithms and improving the cross-domain diagnostic generalization capability of these models is crucial.

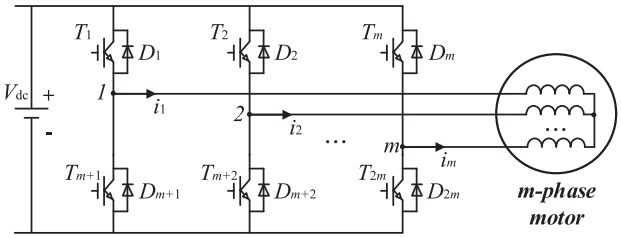

Fig. 1. Structure of m-phase drive system.

To address the deficiencies outlined previously, this article focuses on enhancing normalization preprocessing and integrating deep metric learning (DML) to improve the model's generalization ability for unknown experimental data when trained solely on simulation data. We propose an innovative generalization approach that relies exclusively on simulation data to diagnose faults in multiphase converters. Initially, we reconstruct multiphase currents through normalized data preprocessing, aiming to correct the asymmetry between nonfaulty phase currents and accentuate the distortion characteristics of fault phase currents. This approach seeks to minimize the temporal discrepancies between simulated and experimental data. Subsequently, a 1-D convolutional autoencoder (CAE) network extracts features while ensuring the preservation of the structural integrity of multiphase current signals and mitigating slight temporal variations within the sampling period. Finally, by integrating DML into the classification process, we move beyond the narrow focus on classification accuracy that was prevalent in previous models. This integration also enhances the cohesion among the classes of the features extracted. This technique trains the network model to recognize features with significant discriminative capabilities, enabling precise differentiation among various healthy states. Furthermore, these features exhibit robust clustering properties that alleviate the impacts of nonideal factors in the experimental domain, considerably boosting the network's generalization performance and effectively addressing the challenges of achieving high-performance domain generalization in the absence of experimental fault data.

The contributions of this article are summarized as follows.

1) In response to the challenge of insufficient fault data in experimental domains, this article introduces a domain generalization approach that relies exclusively on simulated data. The method efficiently leverages simulated data for training and demonstrates a high degree of precision in its generalization capabilities when diagnosing real faults.
2) This article presents a normalization preprocessing technique based on the reconstruction of phase currents, which

significantly reduces discrepancies between simulation and experimental data at the network's input layer. This improvement markedly enhances the model's ability to identify different types of faults.

3) The methodology integrates the advantages of DML with classification learning, promoting the aggregation of similar features and thus enhancing the model's clustering ability across various subcategories.

The remainder of this article is organized as follows: Section II provides a detailed description of the proposed method, while experimental verification and comparative analysis are conducted in Section III. Finally, Section IV presents the conclusions drawn from this study.

II. Proposed Method

A. Optimization of Normalization Preprocessing

1) Analysis of Fault Current in Simulation Domain and Experimental Domains: Fig. 1 depicts the circuit topology of a two-level m-phase converter, comprising m parallel bridge arms. Each arm includes two IGBTs ($\{T_k, T_{m+k}, k = 1,2,...,m\}$) and corresponding antiparallel freewheeling diodes ($\{D_k, D_{m+k}\}$) (FWD). During the steady-state phase of a fault, the current of each phase can be effectively modeled by the linear superposition of its respective fault current components, denoted as follows:

$$\left[i_k^F\right] = [i_k] + [f_k] \tag{1}$$

where $[i_k^F]$ denotes the phase currents under fault conditions. $[i_k] = [i_1\ i_2\ \ldots\ i_m]$ are the phase currents in normal operation case and $[f_k] = [f_1 f_2\ \ldots f_m]$ are the fault quantities corresponding to each phase.

For any given phase bridge arm, four distinct states can be identified: normal operation, upper switch fault, lower switch fault, and open phase fault (OPF). When considering an OCF in phase n, an FFT analysis of the current waveform under this condition reveals that the fault component in phase n current can be expressed as follows [22]:

$$f_n = \begin{cases} -I_m \sin\left(\omega t - \frac{2\pi}{m}(n-1)\right), & \text{if OPF} \\ -\frac{1}{2} I_m \sin\left(\omega t - \frac{2\pi}{m}(n-1)\right) + \alpha I_{dc} - \alpha \Delta i_n, & \text{if OSF} \end{cases} \tag{2}$$

where

$$I_{\text{dc}} = \frac{I_m}{\pi}$$

$$\Delta i_n = \sum_{i=1}^{\infty} \frac{2I_m}{\pi\left(4i^2-1\right)} \cos\left[2i\left(\omega t - \frac{2\pi}{m}(n-1)\right)\right]$$

$$\alpha = \begin{cases} -1, & \text{the upper switch is open circuit fault} \\ 1, & \text{the lower switch is open circuit fault.} \end{cases}$$

I_{dc} and Δi_n respectively denote the direct current (dc) component and the even harmonic component within the fault current.

Additionally, a fault in one phase adversely affects the remaining healthy phases by introducing unpredictable fault current components into their respective currents. In multiphase motor systems, increasing the number of phases provides a greater degree of redundant freedom, which typically supports the stability of the fundamental component of the air-gap magnetic field both before and after a fault occurs. Moreover, the motor windings are arranged in a star connection, ensuring that the sum of currents across all phases remains zero. Consequently, a constraint can be derived, referred to as follows:

$$\begin{cases} M^F = M \\ \sum_{j=1}^{m} i_j^F = 0 \end{cases} \tag{3}$$

where M and M^F represent the magnetomotive force (MMF) before and after the fault, respectively.

Given that the MMF comprises both real and imaginary components, the aforementioned three equations result in m-1 indeterminate fault current components f_p ($p = \{1,2,\ldots,m\}$ and $p \neq n$). In theory, this situation could yield an infinite number of solutions. However, the actual distribution of phase currents is uniquely determined. Therefore, investigating supplementary constraints during the fault steady state is imperative to discern the response characteristics of the remaining healthy phase currents under fault conditions.

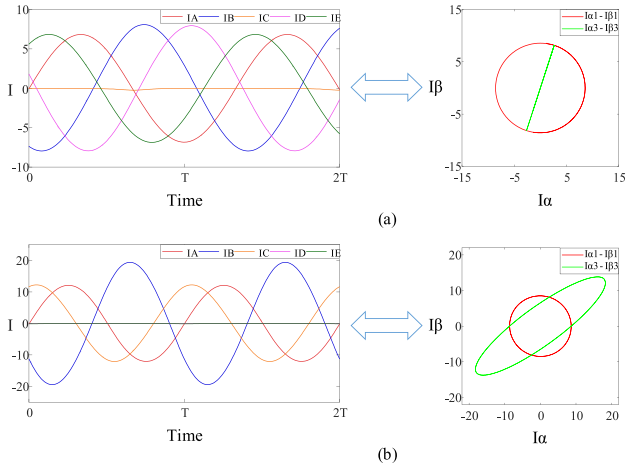

Fig. 2. Trajectory of stator current space vector during OCF of five-phase IM. (a) CASE 1. (b). CASE 2.

Fig. 2 presents the simulation outcomes for a five-phase induction motor (IM) experiencing two fault conditions: a single-phase OCF in phase C (CASE 1) and a two-phase OCF in phases D and E (CASE 2). The figure includes the current waveforms for each phase, as well as the current trajectories on the $\alpha 1$–$\beta 1$ and $\alpha 3$–$\beta 3$ planes. Under these fault conditions, the control system strives to meet torque and flux requirements by maintaining a circular current trajectory in the $\alpha 1$–$\beta 1$ plane, thus ensuring motor stability. In Fig. 2(a), it is evident that following the OCF in phase C, there is a noticeable alteration in the current waveform of the faulted phase, leading to an imbalance in the stator currents of the remaining phases. This imbalance results in a current trajectory on the $\alpha 3$–$\beta 3$ plane forming a horizontal line across the first and third quadrants, rotating around the origin by 72°. Fig. 2(b) reveals that when simultaneous OCF occur in

TABLE I
COEFFICIENT MATRIX OF FIVE-PHASE IM WITH OCF

	Steady-state fault	Minimum loss	Mean absolute error	
	K1	*K2*	$i_{\alpha 3}$	$i_{\beta 3}$
CASE 1	$\begin{bmatrix} -0.2491 & -0.1859 \\ -0.7668 & -0.5720 \end{bmatrix}$	$\begin{bmatrix} -0.2500 & -0.1816 \\ -0.7694 & -0.5590 \end{bmatrix}$	0.89%	0.89%
CASE 2	$\begin{bmatrix} -0.3253 & -2.1293 \\ -0.9624 & -1.3092 \end{bmatrix}$	$\begin{bmatrix} -0.3090 & -2.1266 \\ -0.9511 & -1.3090 \end{bmatrix}$	0.49%	0.45%

phases D and E, the current trajectory on the $\alpha 3$-$\beta 3$ plane takes the shape of an inwardly concave ellipse, centered at the origin and rotated by 36°.

Upon examining the characteristics of these fault conditions and their corresponding current trajectories, a discernible correlation emerges between the harmonic current convergence under steady-state fault conditions and the ideal fault-tolerant trajectory that minimum stator copper losses (ML). More specifically, within the ML constraint, harmonic currents may be approximated as a linear combination of fundamental currents [23]. Furthermore, by applying the least squares method to approximate the ratio of current components across the $\alpha 3$–$\beta 3$ plane relative to the $\alpha 1$–$\beta 1$ plane under steady-state fault conditions, we can derive the corresponding coefficient matrices.

Table I presents the coefficient matrices (***K1*** and ***K2***) under steady-state fault and ML constraints, alongside the differences between the harmonic currents reconstructed using these coefficient matrices and the fundamental current. It indicates that the discrepancy in harmonic currents when employing the ***K1*** matrix is less than 1% relative to those calculated under ML constraints. This consistency can primarily be attributed to the simulation model established in MATLAB/Simulink, which utilizes balanced voltage equations for each phase and assumes symmetrically distributed windings, uniform air gaps, and a sinusoidal MMF distribution. Consequently, the model neglects the contribution of harmonic planes to the rotating MMF, treating harmonic planes solely as a factor of leakage inductance. In this setup, the harmonic planes are effectively positioned in an open-loop state with a reference voltage set to zero. As a result, even if the control strategy remains unchanged, the system can still demonstrate excellent ripple-free post-fault behavior, exhibiting performance akin to that of a reconfigured fault-tolerant strategy [24].

However, it is important to note that nonideal winding distributions, asymmetries during the manufacturing process, spatial harmonics in the air gap, and dead-time effects of the inverter may cause the ideal trajectory of harmonic currents to shift under the OCF condition. Given the relationship between stator phase currents and harmonic currents, as illustrated in (4), any divergence in harmonic current trajectories under *f* steady-state faults between experimental and simulation domains will directly affect the time differences in the phase current waveform, particularly impacting nonfaulty phase currents. In the simulation domain, the waveforms of each phase current align closely with the ML constraint, with nonfaulty phase currents exhibiting unequal effective values that mirror symmetry relative to the position of the faulty phase. Conversely, in the experimental domain, as the waveforms of healthy phase currents deviate from the ML constraint, their symmetry will accordingly alter. For the faulty phase, it will be distributed according to (2) in both the experimental and simulation domains, clearly displaying fault characteristics such as half-wave sinusoids or periodic zeroing

$$i_k^F = \sum_{\rho=1,3,\ldots}^{m-2} \left(i_{\alpha\rho}^F + j i_{\beta\rho}^F\right) * e^{j\frac{2\pi}{m}\cdot\rho(k-1)}, \quad k = 1, 2, \ldots, m \tag{4}$$

where the symbol "$*$" defined as the real part of the product between the first operand and the complex conjugate of the second.

2) Normalization Preprocessing Based on Phase Current Reconstruction: As discussed in the previous section, during steady-state faults, discrepancies in current trajectories on the harmonic plane between the experimental and simulation domains can lead to waveform variations in nonfaulty phases. If these differences are not sufficiently minimized during the data preprocessing stage, the model's generalization ability may be adversely affected. Furthermore, in multiphase motor systems, the fault current components of the remaining healthy phases exhibit significant asymmetry, with the dc bias components of some healthy phases being notably higher than those in traditional three phase systems. This characteristic implies that normalization methods previously effective in fault detection for three phase systems often fail in multiphase systems [25]. To address these challenges, this article introduces a normalization preprocessing approach based on phase current reconstruction. This method aims to reduce the asymmetry among the nonfaulty phases in multiphase motor systems and highlight the distortion characteristics of the faulty phases, thereby minimizing timing differences between the simulation and experimental domains as much as possible. The principle is shown in Fig. 3.

The methodology consists of the following steps.

Step 1: At a constant frequency, sample the current ***I*** and the synchronous speed ω_e of the multiphase motor system under various operational conditions. Determine the current signal's period using ω_e, and execute full-period sliding window sampling

$$T = \frac{2\pi}{\omega_e}. \tag{5}$$

Step 2: Apply (6) to eliminate the asymmetric components in each phase's full-period current signal, thereby restoring balance among the nonfaulty phases. This process not only minimizes sensor noise and other interferences under normal conditions but also effectively removes dc and even harmonic distortions in fault scenarios

$$\bar{I}_i = I_i - \frac{I_{i,\max} + I_{i,\min}}{2} \tag{6}$$

where $I_{i,\max}$ and $I_{i,\min}$ represent the maximum and minimum values of the full-period current signal, respectively.

Step 3: Adjust the amplitude of each phase's current to minimize the impact of variations in motor operational conditions, such as no-load, light-load, and heavy-load changes. Additionally, when the converter experiences an OPF, the fault phase current does not equal zero due to the presence of the FWD

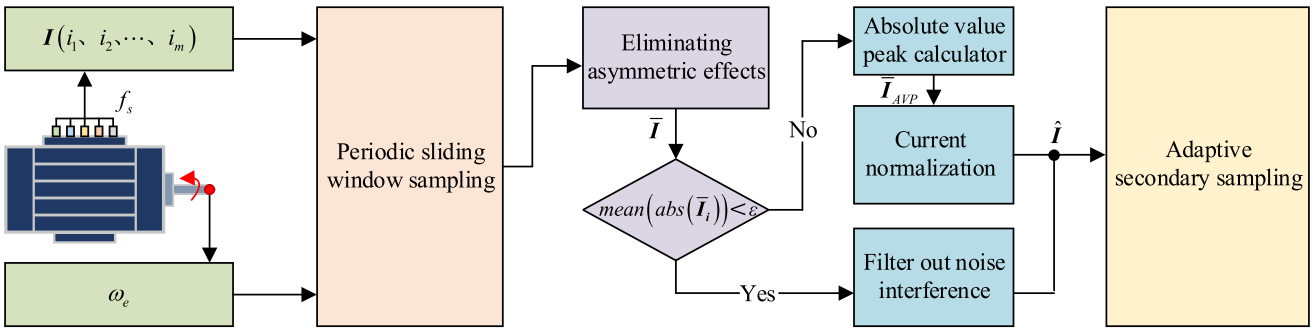

Fig. 3. Schematic diagram of normalized preprocessing based on phase current reconstruction.

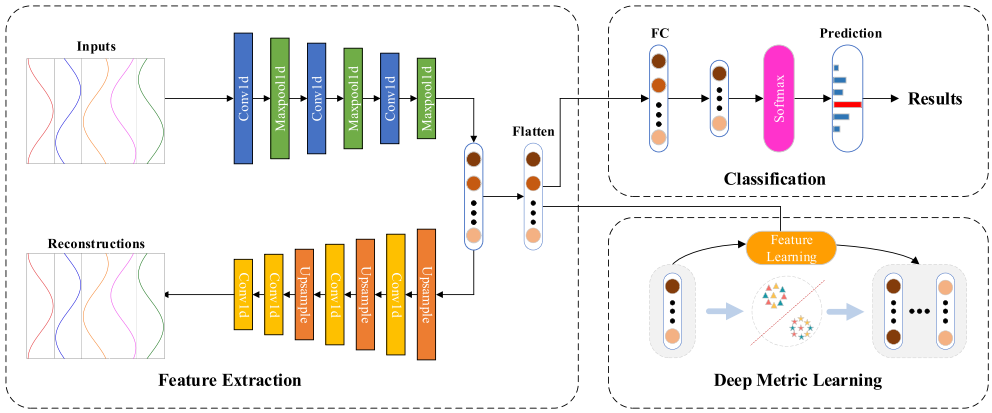

Fig. 4. Overall framework of the proposed model.

[26]. Furthermore, variations in AD sampling accuracy, offset correction, noise interference, and other factors contribute to discrepancies between the nonzero current in the fault phase within the experimental and simulation domains. To prevent further amplification of neighborhood error caused by timing differences in phase current between these domains, we establish an error threshold ε to scale the error. Thus, we represent this relationship as follows:

$$\begin{cases} \hat{I}_i = \frac{\bar{I}_i}{\bar{I}_{i,\mathrm{AVP}}}, \ \mathrm{mean}\left(\mathrm{abs}\left(\bar{I}_i\right)\right) \geq \varepsilon \\ \hat{I}_i = \frac{\bar{I}_i}{100}, \ \mathrm{mean}\left(\mathrm{abs}\left(\bar{I}_i\right)\right) < \varepsilon \end{cases} \tag{7}$$

where $\bar{I}_{i,\mathrm{AVP}}$ represents the absolute maximum value of the full-period current signal after eliminating asymmetrical component.

Step 4: Resolve the disparity between the fixed number of input nodes N_{in} in the deep learning network and the fluctuating count of sampling points during constant frequency operations due to speed variations by implementing equidistant quadratic sampling of the full-period current signal. The selection of the sampling interval is outlined as follows [27]:

$$N_{\mathrm{eqd}} = \frac{T \cdot f_s}{N_{\mathrm{in}} - 1}. \tag{8}$$

B. Integration of Deep Metric Learning

Fig. 4 illustrates the model framework introduced in this paper, which employs an end-to-end learning strategy. The model accepts normalized and preprocessed current signals from a multiphase motor drive system as input and produces fault type labels as output. Notably, this framework integrates DML into the traditional "feature extraction-pattern recognition" approach for fault diagnosis, thereby enhancing the clustering efficacy of individual classification tasks.

1) Feature Extraction and Classification Learning: The design objective of the feature extraction module is to extract meaningful features from multiphase current signals. Research indicates that the CAE, an advanced unsupervised feature learning technology, has been successfully applied to solving feature extraction problems in classification tasks [28]. Motivated by prior studies, this article employs a CAE model to automate feature extraction from multiphase current signals. As shown in Fig. 4, the CAE consists of an encoder with convolutional and pooling layers, as well as a decoder with convolutional and upsampling layers. The CAE utilizes convolution operations to delineate a hidden representation from the input data. Specifically, the encoder processes the input x, converting it into a hidden representation z, expressed as follows:

$$z = \phi\left(\omega x + b\right) \tag{9}$$

where $\phi(\cdot)$ denotes the nonlinear activation function, ω and b represent the weight and bias required to learn, respectively. Subsequently, the decoder reconstructs the output x' from z,

represented as follows:

$$x' = \phi\left(\omega' z + b'\right) \tag{10}$$

where ω' and b' represent the weight and bias required to learn, respectively. For the CAE, the mean squared error loss function is typically employed, as depicted in the following:

$$\text{Loss}_1 = \frac{1}{N}\sum_{i=1}^{N}\|x_i - x_i'\|_2^2 \tag{11}$$

where x_i and x'_i are the ith sample and its approximation, respectively, and N is the number of data samples.

In essence, the encoder convolves input features with a 1-D kernel and an activation function to reduce redundancy and achieve a hidden representation. The decoder then utilizes these features to recreate the initial input through deconvolution operations, further attenuating signal noise. Through this process, CAE-based feature extraction generates a feature mapping from multiphase current signals, which is flattened into a vector and integrated into a fully connected (FC) layer for subsequent processing.

In the proposed model, the features extracted from the CAE are classified using a standard Softmax classifier. The vector z is fed into the FC layer, following by the Softmax layer to compute the predictive probabilities for each health condition, as specified in the following:

$$\hat{y}\left(z\right) = \text{Softmax}\left(\omega'' z + b''\right) \tag{12}$$

where ω'' and b'' represent the weight and bias required to learn, respectively. The model parameters are subsequently updated to minimize the cross-entropy (CE) loss, calculated as follows in

$$\text{Loss}_2 = -\sum_{k=1}^{N} y_k \log \hat{y}_k \tag{13}$$

where y_k are $\hat{y}_k$ the true labels and the classification possibilities separately. Finally, the model's performance is evaluated by calculating the CE loss to estimate the discrepancies between the predicted outputs and the actual labels.

2) Deep Metric Learning: By utilizing phase current reconstruction for normalized preprocessing, this article minimizes temporal discrepancies between simulation and experimental domain data. However, this approach does not guarantee effective clustering across different categories, making the model susceptible to noise and domain shifts, which ultimately diminish its generalization capability in experimental domains. To address these issues, this paper integrates DML into our classification approach. Unlike traditional classification tasks, DML focuses on creating a discriminative and cohesive feature space by learning data similarities. This technique enhances the model's generalization by fostering intraclass cohesion and interclass separability.

Specifically, the feature representation $F(x)$ is regularized to reduce intraclass distances while increasing interclass distances. In this context, intraclass clustering compactness is quantified as $\text{Loss}_{\text{intra}}$, defined as follows:

$$\text{Loss}_{\text{intra}} = \frac{1}{C}\sum_{c=1}^{C}\frac{1}{N_c D}\sum_{j=1}^{N_c}\left\|\bar{F}\left(x^c\right) - F\left(x_j^c\right)\right\|_1 \tag{14}$$

$$\bar{F}\left(x^c\right) = \frac{1}{N_c}\sum_{i=1}^{N_c} F\left(x_i^c\right) \tag{15}$$

where x^c denotes a sample of the cth health condition in the training data, and x_j^c denotes the jth sample in x^c, N_c is the number of x^c, D denotes the dimension of advanced feature representation $F(x)$, C is the number of health condition, $\bar{F}(x^c)$ is the average value of $F(x_i^c)$, and $||\cdot||_1$ is the first-order norm. At the same time, interclass separability is quantified as $\text{Loss}_{\text{inter}}$, defined as follows:

$$\text{Loss}_{\text{inter}} = \frac{1}{CD}\sum_{c=1}^{C}\left\|\tilde{F}\left(x\right) - \bar{F}\left(x^c\right)\right\|_1 \tag{16}$$

$$\tilde{F}\left(x\right) = \frac{1}{C}\sum_{c=1}^{C}\bar{F}\left(x^c\right) \tag{17}$$

where $\tilde{F}(x)$ denotes the mean of $F(x^c)$ in different classes. Ultimately, by combining $\text{Loss}_{\text{intra}}$ and $\text{Loss}_{\text{inter}}$, the distance-based DML loss function can be encapsulated as follows:

$$\text{Loss}_3 = \text{Loss}_{\text{intra}} - \text{Loss}_{\text{inter}}. \tag{18}$$

C. Overall Framework

During the model training process, this article emphasizes minimizing the classification loss (Loss_2) associated with health status by optimizing both the encoder within the feature extraction module and the classifier within the classification learning module. Simultaneously, the encoder aims to reduce the distance metric loss (Loss_3) in the DML module. Additionally, the decoder in the feature extraction module is updated to minimize the reconstruction loss (Loss_1) in accordance with the data reconstruction strategy. As a result, the network optimization problem can be expressed as follows:

$$\begin{aligned}\hat{\theta}_E &= \arg\left\{\min_{\theta_E}\text{Loss}_1, \min_{\theta_E}\text{Loss}_2, \min_{\theta_E}\text{Loss}_3\right\}\\ \hat{\theta}_D &= \arg\min_{\theta_D}\text{Loss}_1, \hat{\theta}_C = \arg\min_{\theta_C}\text{Loss}_3\end{aligned} \tag{19}$$

where θ_E, θ_D, and θ_C denote the parameters of encoder, decoder, and classification, respectively. The optimization problem can be effectively solved using the adaptive moment (Adam) estimation algorithm, enabling the optimization of parameters as represented by the following:

$$\begin{aligned}\theta_E^{t+1} &\leftarrow \theta_E^t - \eta^t\left(\frac{\partial\text{Loss}_1}{\partial\theta_E} + \frac{\partial\text{Loss}_2}{\partial\theta_E} + \frac{\partial\text{Loss}_3}{\partial\theta_E}\right)\\ \theta_D^{t+1} &\leftarrow \theta_D^t - \eta^t\frac{\partial\text{Loss}_1}{\partial\theta_D}, \theta_C^{t+1} \leftarrow \theta_C^t - \eta^t\frac{\partial\text{Loss}_3}{\partial\theta_C}\end{aligned} \tag{20}$$

where η^t is the learning rate at the tth iteration. The algorithm for the proposed model framework is detailed in Algorithm 1.

Algorithm 1

Data Pre-processing Stage

1: Whole-cycle sliding window sampling by (5)
2: Normalization preprocessing based on phase current reconstruction by (6) and (7)
3: Adaptive secondary sampling by (8)

Training Stage and Verification Stage

Require: Train data D^S_{train}, D^E_{train} and Verification dataD^S_{ver}, D^E_{ver} from simulation domain and experimental domain, the number of fault types C, the batch size B, the number of traing steps n_{step}, the learning rate η
Module: The untrained networks E, D, and C
Return: The trained network E, D, and C
1: Initialization: θ_E, θ_D, and θ_C
2: **for** $t = 1,2,\ldots,n_{step}$ **do**
3: **1)** Training
4: **1.1)** Randomly sample a batch of data $\{(x_j^{train}, y_j^{train})|j = 1, 2, \cdots, B\}$ from D^S_{train}
5: **1.2)** Forward propagation of the network
6: Calculate the reconstruction loss $Loss_1$ by (11)
7: Calculate the classification loss $Loss_2$ by (13)
8: Calculate the distance metric learning $Loss_3$ by (18)
9: **1.3)** Backpropagation
10: Update the parameters of by E, D, and C by (20)
11: **2)** Verification
12: **2.1)** Randomly sample a batch of data $\{(x_j^{ver}, y_j^{ver})|j = 1, 2, \cdots, B\}$ from D^S_{ver}
13: **2.2)** Evaluate the pre-trained model and save the best parameters
14: end for

Test Stage

Require: Test data D^S_{test}, D^E_{test} from simulation and experimental domain
Module: The trained networks E and C in the training stage
Return: The predicted labels y^S_{test} and y^E_{test}
1: **for** $\mathrm{D_{test}} = \mathrm{D^S_{test}}$, $\mathrm{D^E_{test}}$ **do**
2: **for** each x_j^{test} in $\mathrm{Dtest} = \{x_j^{test}|j = 1, 2, \cdots, N_{test}\}$ **do**
3: $y_j^{test} = \mathrm{argmax}(C(E(x_j^{test})))$
4: **end for**
5: end for

III. Experimental Verification and Comparison Analysis

A. Data Acquisition

To verify the effectiveness of the proposed cross-domain fault diagnosis method for OCF in multiphase converters, we constructed a five-phase IM drive system in the laboratory to collect experimental domain datasets. This system featured a symmetric winding arrangement, with a 72° electrical angle separation between adjacent phases. Details of the experimental platform and its electrical specifications are depicted in Fig. 5. Furthermore, we utilized MATLAB/Simulink to create a simulation model of the motor drive that replicated the parameters of the experimental setup, thereby enabling the acquisition of simulation domain data. Additionally, both the motor drive system in the experimental domain and the simulation domain employ a control method that combines fundamental plane closed-loop control with harmonic plane open-loop control.

Given that a five-phase motor can accommodate faults in up to two phases, we collected data under various conditions, including normal operation, an OCF in the upper switch of phase A, an OCF in the lower switch of phase A, an OPF in the phase A, simultaneous faults in the upper switches of phases A and B, and simultaneous faults in the lower switch of phase A and bridge arm of phase C. To clarify the descriptions, the abbreviations OP(f), OUS(f), and OLS(f) denote the OPF, upper switch OCF, and lower switch OCF in the fth phase, respectively. Consequently, these faults are designated as OUS(A), OLS(A), OP(A), OUS(A)&OUS(B), and OLS(A)&OP(C). In the simulation domain, we collected 1152 sets of class-balanced data, which were divided into training, validation, and simulation domain test sets in the ratios of 7:3:2. In the experimental domain, we gathered a similar number of datasets, used exclusively as experimental domain test data. Various working conditions such as speed, and load torque variation are considered in data acquisition with regard to different fault types, as shown in Table II.

Fig. 6 illustrates the detailed composition of these datasets. With this division, the training and validation sets comprised solely of simulation domain data were employed for model training and parameter tuning. Furthermore, the simulation domain test set was used to assess whether the model exhibits overfitting on the simulation domain data, thereby ensuring the model's stability. By using the experimental domain test set, we can comprehensive evaluation of the model's cross-domain fault diagnosis generalization performance.

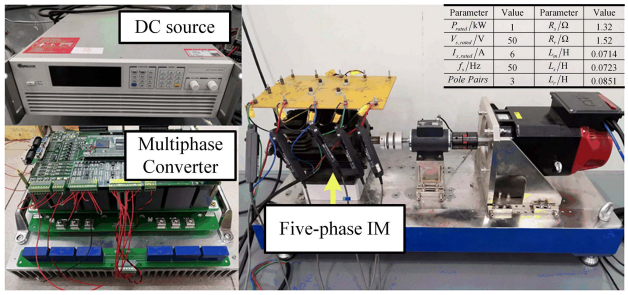

Fig. 5. Five-phase IM drive platform.

TABLE II
Simulation and Experimental Data Acquisition

Parameters	Simulation domain	Experimental domain
Rated speed	3 (600:1000/200 r/min^{-1})	8 (300:1000/100 r/min^{-1})
Rated load torque	4 (0:9/3 N·m)	11 (0:12/1.2 N·m)

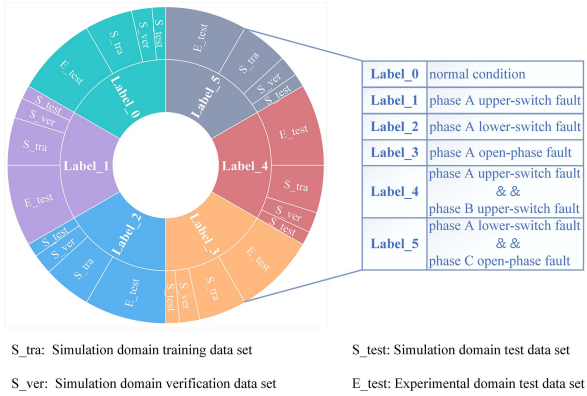

Fig. 6. Composition of the dataset.

TABLE III
STRUCTURAL PARAMETERS OF THE NETWORK MODEL

	Layer	Parameter	Activation	Output shape
Encoder	Conc1d+BN	(5,16,16)	LReLU	(16,16,113)
	MaxPool1d	2	-	(16,16,56)
	Conc1d+BN	(16,32,4)	LReLU	(16,32,53)
	MaxPool1d	2	-	(16,32,26)
	Conc1d+BN	(16,32,4)	LReLU	(16,32,23)
	MaxPool1d	2	-	(16,32,11)
	Flatten	-	-	(16,352)
Decoder	Upsample	2	-	(16,32,22)
	Conv1d+BN	(16,32,3)	LReLU	(16,32,26)
	Upsample	2	-	(16,32,52)
	Conv1d+BN	(32,16,3)	LReLU	(16,16,56)
	Upsample	2	-	(16,16,112)
	Conv1d+BN	(16,16,15)	LReLU	(16,16,128)
	Conv1d+BN	(16,5,15)	-	(16,5,128)
Classifier	Linear	(352,50)	-	(16,50)
	Linear	(352,6)	SoftMax	(16,6)

B. Parameters Setting

Table III presents the structural parameters for the encoder, decoder, and classification components within the network model. The data sample length was set to 128, with each training batch comprising 16 samples, and a total of 50 computational iterations were completed. Set the initial learning rate to 0.001, and determine the error threshold ε as 0.2 based on experimental evaluation and operational conditions. To improve model convergence, a learning rate decay strategy was implemented. An Adam optimizer with weight decay regularization was utilized during training iterations to minimize the loss function, effectively optimizing the network's learnable parameters. Ultimately, the model that exhibited the lowest loss and highest accuracy on the validation set was selected as the optimal model for further testing and diagnostic applications in both simulation and experimental domains.

C. Experimental Results

1) Offline Training Results:

a) Influence of normalized preprocessing method on model discriminant performance: Figs. 7 and 8 illustrate the changes in phase current waveforms before and after preprocessing in the simulation domain and the experimental domain under OUS(A) and OP(A) fault conditions. A pronounced difference was observed in the performance of the remaining healthy phases between these two domains prior to normalization preprocessing. Specifically, in the simulation domain, the stator phase current during the fault steady state was influenced by optimization constraints similar to those encountered in fault-tolerant control, which resulted in a mirror-symmetrical feature relative to the faulty phase. In contrast, the non-faulty phase current in the experimental domain, affected by factors such as motor parameter characteristics, did not exhibit the expected theoretical symmetry found in the simulation domain, leading to inconsistently unpredictable differences among the phase currents.

Notably, the normalization preprocessing technique proposed in this study significantly reduced the asymmetry among nonfaulty phases. Table IV presents the polar Euclidean distances

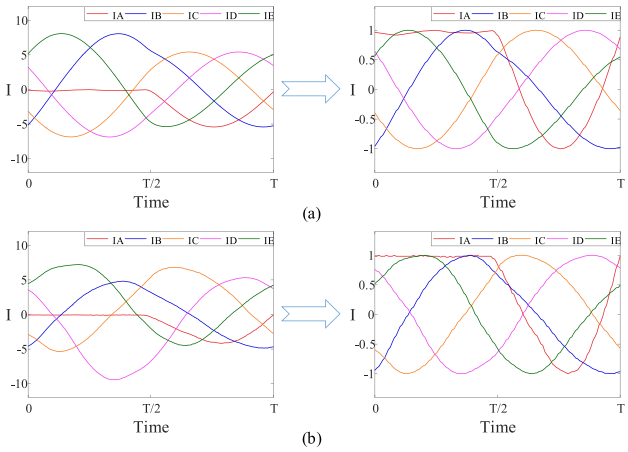

Fig. 7. Comparison diagram of steady-state current waveform before and after normalized pretreatment of OUS(A). (a) Simulation domain. (b) Experimental domain.

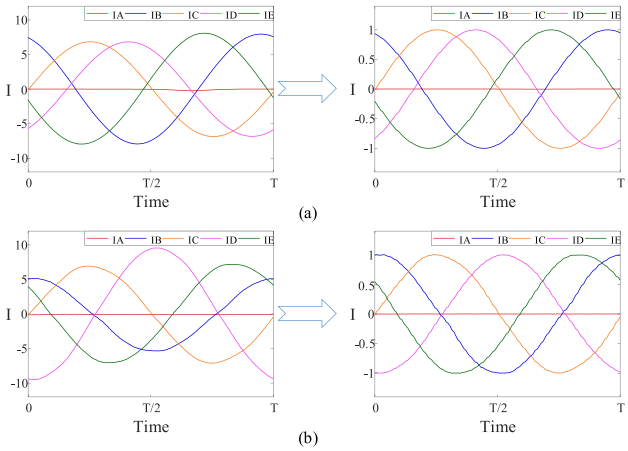

Fig. 8. Comparison diagram of steady-state current waveform before and after normalized pretreatment of OP(A). (a) Simulation domain. (b) Experimental domain.

TABLE IV
POLAR EUCLIDEAN DISTANCE

		Phase B	Phase C	Phase D	Phase E
OUS (A)	Before pretreatment	3.40	4.19	4.72	2.99
	After pretreatment	0.29	2.18	1.74	2.20
	Decrease value	↓91%	↓48%	↓63%	↓26%
OP (A)	Before pretreatment	5.33	0.99	10.01	8.81
	After pretreatment	3.36	0.31	5.63	5.99
	Decrease value	↓37%	↓68%	↓44%	↓32%

(PED) [28] of nonfaulty phase currents before and after preprocessing under both fault conditions in the simulation and experimental domains. A PED value near 0 indicates a high degree of similarity in magnitude and phase between the two current vectors. The data presented in the table reveal that nonfaulty phase currents not subjected to preprocessing exhibited considerable disparity between the simulation and experimental domains. For instance, the D phase in OUS(A) had a PED value of 4.72, while the E phase in OP(A) had a value of 8.81.

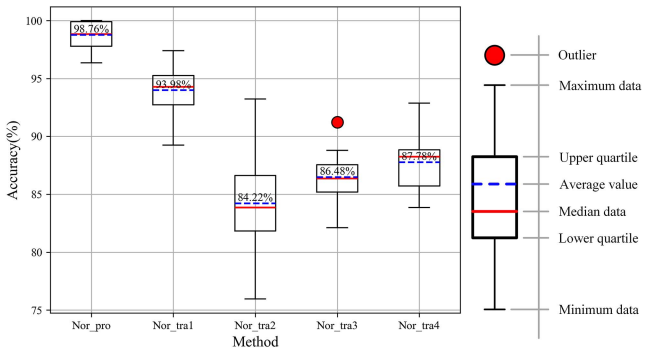

Fig. 9. All accuracies of each normalized preprocessing methods.

However, these differences were notably alleviated after normalization preprocessing based on phase current reconstruction. In OUS(A), the PED value for the D phase reduced to 1.74, marking a 63% decrease. In OP(A), the PED value for the E phase dropped to 5.99, representing a reduction of 32%. These results indicate a significant reduction in the degree of asymmetry among nonfaulty phases within the specified domains. Concurrently, the amplitudes of phase current waveforms in both domains were balanced, and skewness in data distribution across neighboring areas was mitigated. Although the PED values of corresponding phase currents in both domains did not entirely converge to 0 after preprocessing, primarily because the main focus of preprocessing was on current amplitude equalization, minor phase discrepancies were still observed. Nevertheless, the multichannel convolutional operations of the CAE network employed in this study demonstrated robustness in handling minor time shifts in the periodic signal samples.

To demonstrate the superiority of our approach (Nor_pro), we compared it with commonly used signal processing normalization techniques, including Park's vector modulus (Nor_tra1) [29], absolute maximums (Nor_tra2) [30], and traditional statistical normalization methods such as Min-Max Scaling (Nor_tra3) [31] and Standardization (Nor_tra4) [32]. To ensure a fair assessment, the experiments utilized a basic model of "feature extraction-pattern classification" (CAE-Classify) to eliminate potential influences from the DML module. The dataset was constructed from randomly selected samples from a large database, and 20 repeated tests were conducted. The experimental results are shown in Fig. 9, where the blue dashed line represents the average accuracy and the red solid line represents the median accuracy. The data indicate that our method significantly outperforms the others, achieving average and median accuracies of 98.76% and 98.82%, respectively, and surpassing the next best method by approximately 5%. Additionally, our method exhibited the least accuracy fluctuation and the shortest box length, indicating excellent stability across repeated experiments. In contrast, other methods showed certain disadvantages in various indicators, such as the larger box length of Nor_tra2 and a higher dispersion of accuracy. Notably, Nor_tra3 showed outliers, suggesting that this normalization method might introduce bias in the test set accuracy. Through the assessment of concentration trends, dispersion, and the occurrence of outliers in the experimental domain accuracy under various normalization preprocessing methods, it can be concluded that our method offers advantages of high stability, low fluctuation, and no outliers.

Moreover, we analyzed the impact of different normalization methods on the classification of various health conditions, with results presented in the confusion matrix in Fig. 10. By observing the recall rates and shades of color on the main diagonal, it is evident that our method demonstrates exceptional performance across all categories, effectively capturing true fault samples and significantly reducing missed diagnoses. Conversely, the other methods exhibited varying misdiagnosis rates across categories due to insufficient consideration of motor parameter characteristics and the symmetric relationships between nonfaulty phase currents, resulting in suboptimal performance on untrained experimental domain test sets. For instance, the Nor_tra1 method applies the modulus of current vectors as the scaling factor for all phase currents, neglecting the asymmetric relationships among the nonfaulty phases. Consequently, it sometimes misclassifies OLS(A) as either normal or OLS(A)&OP(C). In contrast, the Nor_tra2 method employs the maximum absolute values of each phase current as respective scaling factors. However, it fails to rectify the asymmetric conditions resulting from asymmetrical component, leading to frequent confusion between OLS(A) and OLS(A)&OP(C). Given that the Nor_tra3 and Nor_tra4 methods normalize input signals solely based on statistical metrics, while ignoring the physical properties inherent in the currents, these approaches fall short in enhancing the symmetric relationship between non-faulty phases. Furthermore, they overlook uncertainties such as AD sampling accuracy, offset correction, and noise interference, resulting in a recall rate below 50% for detecting OP(A).

These results further corroborate that our proposed method reduces discrepancies in phase current time sequences under various fault conditions, thereby enhancing the model's generalization performance for neighborhood fault diagnosis. It is noteworthy that the above analysis primarily targets the experimental domain test set. We found that in repeated experiments, the fault diagnosis accuracy of the simulation domain test set consistently remained at 100%, unaffected by the normalization preprocessing methods. This indirectly validates the effectiveness of the model architecture used in this article for feature extraction and its generalizability in independent and identically distributed datasets within the simulation domain, without exhibiting overfitting phenomena.

b) Influence of deep metric learning on model clustering performance: In analyzing the confusion matrix from the preceding section, we discovered that the baseline model misclassified some samples of OUS(A)&OUS(B) as those belonging to OUS(A), resulting in a misdiagnosis rate of 7.81%. Additionally, the overall accuracy in the experimental domain test set was 98.76%, which did not reach the perfect accuracy of 100% attained in the simulation domain test set. These findings suggest that while the baseline model is proficient at extracting features from preprocessed signals and achieves superior performance through a well-structured training strategy, its primary focus lies in learning discriminative features while neglecting

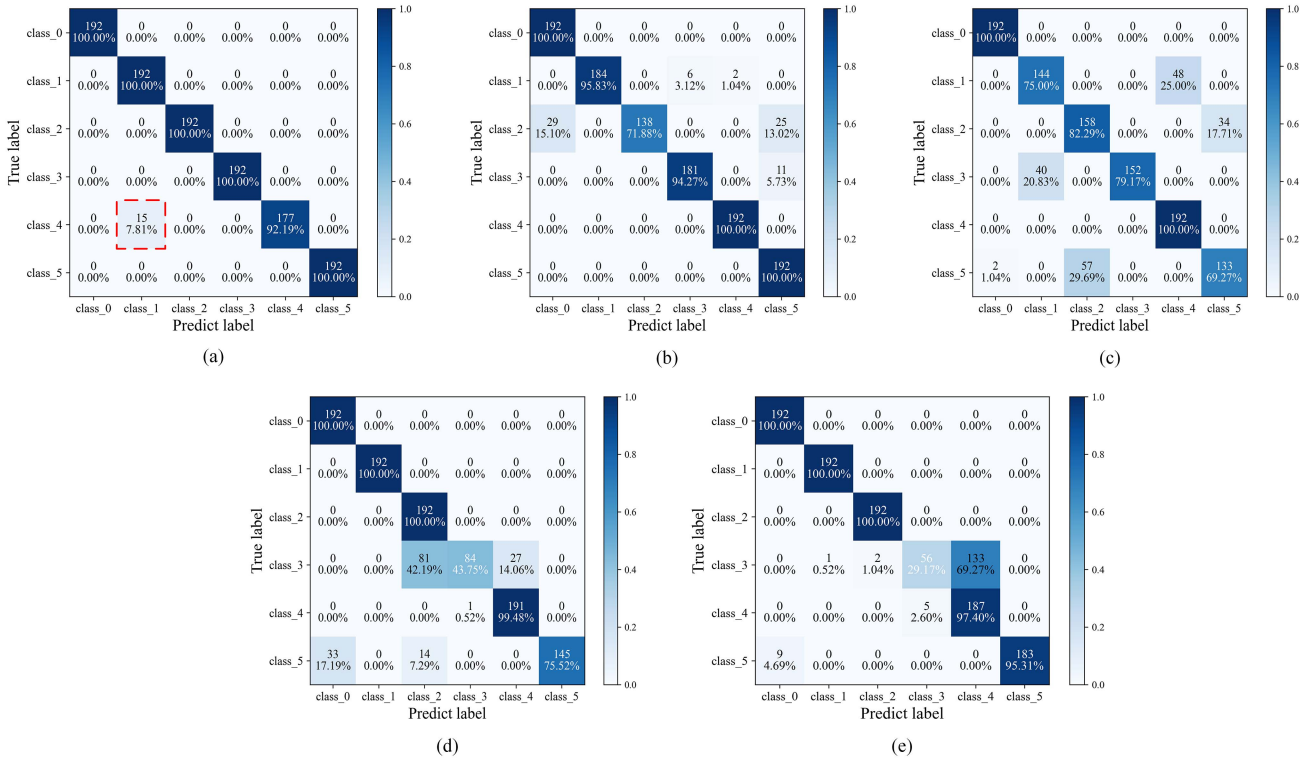

Fig. 10. Confusion matrix of each normalized preprocessing methods (a) Nor_pro, (b) Nor_tra1, (c) Nor_tra2, (d) Nor_tra3, (e) Nor_tra4.

TABLE V
EVALUATION INDEX OF EACH MODEL

Method	Accuracy	Precision	Recall
Proposed model	0.9958	0.9961	0.9958
Baseline model	0.9876	0.9891	0.9876

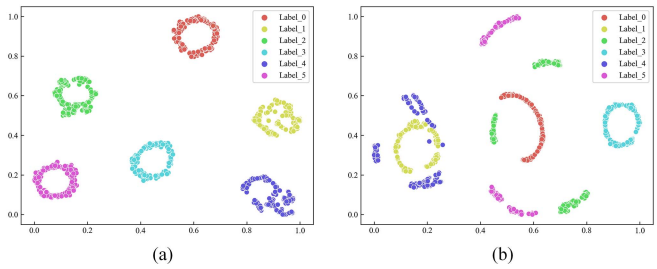

Fig. 11. Visualization results on the experimental domain test set. (a) Proposed model. (b) Base model.

characteristics associated with clustering. To address this shortfall, the present research integrates DML with classification tasks, aiming to enhance the model's generalizing capability by learning feature representations with pronounced clustering characteristics.

To validate the effectiveness of our proposed "CAE-Classification+Metric" model (hereinafter referred to as the proposed model), we conducted benchmark tests on the "CAE-Classification" model (hereinafter referred to as the baseline model) using the same dataset. We utilized three core evaluation metrics, accuracy, precision, and recall, to thoroughly assess the performance of the models across different subcategories and overall situations. The performance of both the proposed model and the baseline model across these metrics is summarized in Table V. The proposed model achieved an accuracy of 0.9958, surpassing the baseline model's 0.9879, indicating its superior ability to accurately judge the fault categories of samples overall. The precision of the proposed model was 0.9961, significantly higher than the baseline model's 0.9876, demonstrating its near-absence of misjudgments in fault identification and effectively minimizing misdiagnoses. In terms of recall, the proposed model also outperformed the baseline model, achieving a performance score of 0.9958 compared to the baseline's 0.9876. This indicates that it maximizes the identification of all potential faults while reducing missed diagnoses. In summary, the proposed model outperforms the baseline model across all key evaluation metrics, validating its ability to identify fault samples more accurately while maintaining lower rates of misjudgments and missed diagnoses, thus exhibiting better overall performance.

To further assess the effectiveness of DML in capturing cluster-characteristic features, we utilized t-distributed stochastic neighbor embedding (t-SNE) to visualize the high-dimensional features extracted from both models within the experimental domain's test set, as shown in Fig. 11. The visualization reveals that within the proposed model, samples representing different health statuses cluster closely around

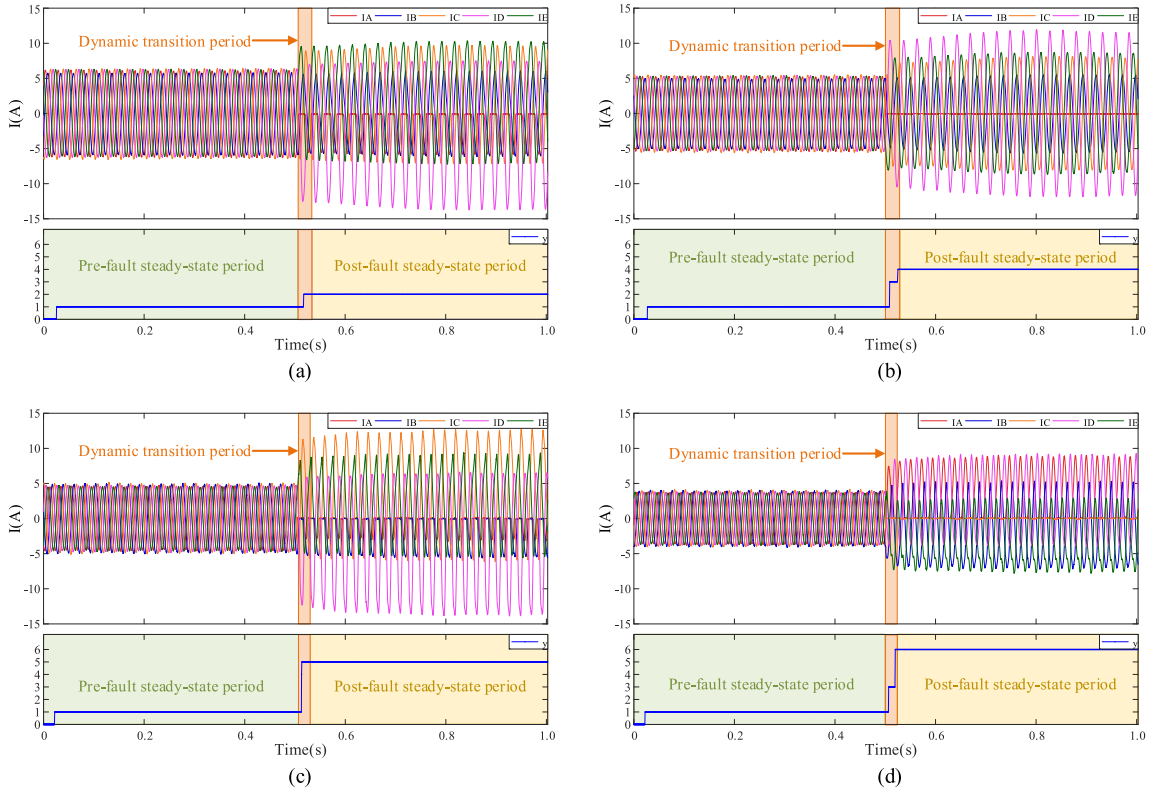

Fig. 12. Real-time experimental results of fault diagnosis. (a) OUS(A). (b) OP(A). (c) OUS(A)&OUS(B). (d) OLS(A)&OP(C).

TABLE VI
FEATURE QUANTITATIVE EVALUATION OF EACH MODEL

Method	Experimental domain test set-J		
	Mean	Max	Min
Proposed model	7.35	8.42	5.94
Baseline model	3.81	4.08	3.47

their category's central position in the feature space, delineating clear boundaries among these statuses. Conversely, the baseline model, despite exhibiting no overlap among normal, OLS(A), and OLS(A)&OP(C), fails to demonstrate a distinct clustering structure, showing notably poor intraclass compactness. Notably, overlaps between samples of OUS(A) and OUS(A)&OUS(B) suggest greater classification challenges for these categories, potentially leading to misjudgments, which explains the 7.81% misjudgment rate.

Moreover, we introduced a quantitative evaluation index J, that gauges a feature's clustering capability by comprehensively analyzing the within-class and between-class scatter matrices [33]. Higher J values indicate an enhanced clustering ability, characterized by more pronounced interclass dispersion relative to intraclass dispersion, aiming to minimize distances within classes while maximizing distances between them. Table VI details the comparison of feature quantitative evaluation results for both models in the test set of the experimental domain. Here, the proposed model significantly outperformed the baseline model across all statistical metrics, with its average J value, maximum J value, and minimum J value exceeding those of the baseline model by 92.77%, 106.15%, and 71%, respectively. This evidence suggests that DML significantly enhances feature clustering capability and model generalization by effectively decreasing intraclass distances and increasing interclass distances.

2) Online Diagnosis Results: To substantiate the proposed method's feasibility, we evaluated the online diagnostic performance of the pretrained network on a five-phase IM drive system. During the online phase, current signals from each phase within the experimental domain were sampled using a sliding window with a length equivalent to one fundamental period (FP) T. To balance the algorithm's initiation frequency and the timeliness of diagnostic responses, a sliding step size of T/40 was selected. The collected data were subsequently fed into the deployed pretrained network for fault diagnosis.

Fig. 12 illustrates the real-time results of online diagnostics under four fault conditions: OUS(A), OP(A), OUS(A)&OUS(B), and OLS(A)&OP(C). The variable y serves as the fault diagnosis indicator, where y = 1, 2, 3, 4, 5, and 6 correspond to normal operation, OUS(A), OLS(A), OP(A), OUS(A)&OUS(B), and OLS(A)&OP(C), respectively. A value of $y = 0$ indicates that the algorithm is still collecting data and has not yet completed the diagnosis. Given that the input signals for the diagnostic algorithm proposed in this paper are full-period current signals, the duration of the $y = 0$ state is approximately one FP. From a practical industrial application perspective, we define the time period starting from the moment a fault is triggered and lasting for one FP as the "dynamic transition period" [34]. During this interval, the system has not yet reached the steady-state fault stage, and the input signals obtained through

TABLE VII
ONLINE DIAGNOSTIC RESPONSE PERFORMANCE

Fault types	Fundamental period	Fault trigger	Fault diagnosis		Diagnostic response
			Fault detection	Fault localization	
OUS(A)	0.02545 s	0.5073 s	0.5175 s	0.5175 s	40.08%
OP(A)	0.02645 s	0.5011 s	0.5088 s	0.5252 s	91.11%
OUS(A)&OUS(B)	0.02155 s	0.5049 s	0.5131 s	0.5146 s	45.01%
OLS(A)&OP(C)	0.02174 s	0.5011 s	0.5068 s	0.5198 s	86.02%

sliding window sampling contain data from both healthy and fault states. Since the input signals used during offline network training comprise solely steady-state data, instances of misdiagnosis may occur during online real-time diagnostics within the dynamic transition period. This phenomenon is expected for supervised deep learning systems [35]. For example, as shown in Fig. 12(b), during the dynamic transition period, the data obtained from the A-phase current through the sliding sampling window contains both the sinusoidal upper half wave of the healthy state and the constant zero value of the fault state. Consequently, the network may easily diagnose this sample as OLS(A). However, aside from the dynamic transition period, the network model's output remains stable and reliable during both the prefault and postfault steady-state phases.

Table VII illustrates the response performance of online fault diagnosis systems under four distinct fault conditions. "Fault detection" denotes the moment when the fault indicator $y = 0$ exhibits a sudden change. "Fault localization" refers to the moment at which the fault indicator y transitions to its corresponding label. "Diagnostic response" is defined as the ratio of the diagnosis time to the FP, indicating the diagnostic speed of the strategy. It is important to note that the diagnosis time is counted based on the failure of the device in the effective half cycle of the inverter operation [36]. For example, the upper switch of the bridge arm fails in the positive half cycle of the inverter output. The table reveals that the proposed diagnostic strategy responds rapidly to fault categories such as OUS(A) and OUS(A)&OUS(B), which do not involve OPF, typically within 0.5 FP. Conversely, for fault categories that include OPF, such as OP(A) and OLS(A)&OP(C), the response is slower, generally around 0.9 FP. Although the data-driven intelligent fault diagnosis strategy proposed in this paper may be slightly slower in terms of diagnostic speed compared to methods based on signal processing or model prediction, it offers significant advantages. Specifically, it circumvents the need for analyzing circuit operational mechanisms, developing precise circuit models, and formulating diagnostic rules and thresholds. Moreover, transitioning to a fault-tolerant operational state after one FP helps prevent damage to multiphase motor drive systems, thereby satisfying the requirements of most application scenarios [3].

3) Generalization Performance Verification:

a) Different motor parameters: To validate the generalization capability of the proposed method for motor systems with differing parameters, we substituted the parameters of Motor A used in this study with those of Motor B, as detailed in [37], during the simulation modeling of a five-phase IM. We then randomly selected various operating conditions for the simulation to gather a comprehensive dataset. The network model was subsequently trained using the simulation data from Motor B, and the optimal model was evaluated based on its accuracy on the validation set. The pretrained optimal network model was later applied to the experimental data from Motor A.

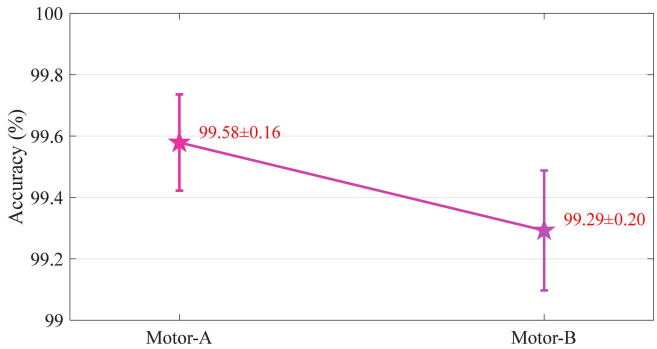

Fig. 13. Comparison of motor parameters generalization performance.

Fig. 13 illustrates the diagnostic accuracy of the pre-trained optimal network model using simulation data from both Motor A and Motor B when tested on the experimental dataset of Motor A. The results demonstrate that the model pretrained with simulation data from Motor A achieved a diagnostic accuracy of 99.58%, while the model pretrained with data from Motor B attained an accuracy of 99.29% on the same dataset. Although there are minor discrepancies between the two results, both accuracies exceed 99%. Therefore, the intelligent fault diagnosis method based on prior knowledge proposed in this article effectively applies the pretrained diagnostic model to new systems with different electrical parameters, eliminating the need for multiple training sessions with new experimental data and showcasing strong migration ability. This method addresses the limitation of existing machine learning models, which, when trained on a single fault database, can only be applied to specific systems and struggle to accurately generalize to other systems with the same topology but differing parameters.

b) Different motor types: To validate the applicability of the proposed method across various motor systems, we applied it to the dual three-phase PMSM available in our laboratory [38]. The dual three-phase PMSM is an asymmetric multiphase motor system that complements symmetric multiphase systems, such as the five-phase IM. Since single-switch OCF and single-phase OCF are the most common and representative fault types, and considering that the dual three-phase motor with isolated neutral points can be viewed as two symmetrical three-phase motor systems. This article focuses on single-switch faults and open-phase fault of phase A as a case study for data collection.

TABLE VIII
COMPARISON WITH RELEVANT APPROACHES

Relevant diagnosis approach	Diagnostic variable	Fault types	Offline accuracy	Online diagnosis time	Requirements			
					R1	R2	R3	R4
[39]	Current_α_1-β_1	Phase	—	≈ 1.125 FP	Yes	No	No	No
[40]	Current_phase and Gate drive signals	Phase / Switch	—	≈ 0.020 FP	Yes	Yes	Yes	No
[42]	Current_α_3-β_3	Phase	97.19%	—	Yes	Yes	—	No
[43]	Current_d_1	Phase	96.40%	—	Yes	No	—	No
[35]	Current_α_1-β_1	Phase	97.40%	≈ 1.667 FP	Yes	Yes	—	No
This method	Current_phase	Phase / Switch	99.58%	⩽ 0.911 FP	Yes	Yes	Yes	Yes

Note: The above comparison is only for five-phase motor. "—" stands for not provided in the literature.

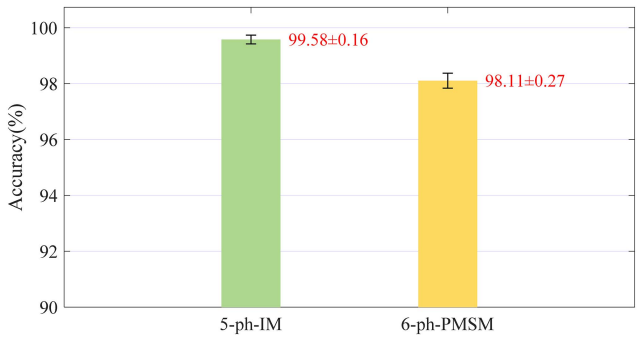

Fig. 14. Comparison of motor types generalization performance.

Fig. 14 illustrates the diagnostic accuracy of the experimental domain test set for both the five-phase IM and the dual three-phase PMSM. The diagnostic accuracy of the fault diagnosis strategy proposed in this paper is 98.11% for the dual three-phase PMSM, which is slightly lower than the 99.58% accuracy observed in the five-phase IM. Analysis suggests that this discrepancy is primarily attributable to the presence of low-order harmonic components in the phase current of the dual three-phase PMSM under healthy conditions in the experimental domain, while the phase current in the simulation domain closely approximates a sine waveform. The main input feature identified by the best model trained on simulation domain data in a healthy state is the fundamental frequency component. However, when this model is applied to unknown experimental domain test data, the low-order harmonic components introduce low-frequency noise. As these noises resemble the primary feature (the fundamental frequency component), they are susceptible to aliasing, which adversely affects the model's identification capability. Nonetheless, in application scenarios where experimental data are scarce, it remains acceptable for a model trained exclusively on simulation data to achieve diagnostic accuracy exceeding 98% on unknown experimental data. This finding underscores the broad applicability of the proposed method across different types of multiphase motor systems.

4) Performances Comparison: Table VIII provides a comparative evaluation of the developed technique against other data-driven fault diagnosis methods for multiphase motor drive systems, emphasizing its superiority and effectiveness. Before analyzing Table VIII, it is essential to understand several key characteristics of data-driven fault diagnosis strategies.

(R1) Utilization of noninvasive techniques that do not additional hardware (e.g., voltage sensors).

(R2) Independence from varying operating conditions (e.g., load values, speed values, etc.).

(R3) Independence from machine parameters and/or control strategies.

(R4) Capability to address issues related to data scarcity while demonstrating certain generalization characteristics.

Olivieri [39] designed a feedforward neural network to identify OCF in five-phase PMSM. This strategy requires 1.125 FP for online diagnosis and can only detect single-phase OCF. Furthermore, it is susceptible to changes in load changes and variations in control strategies. Torabi et al. [40] employed a self-recurrent wavelet neural network for nonlinear modeling of converters in five-phase IM drive systems. This approach predict motor currents corresponding to health conditions, enabling fault detection in under 1 ms. However, this hybrid strategy often necessitates a high control frequency, which increases both the algorithm initiation frequency and computational load, resulting in higher memory consumption [41]. Shao et al. [42] utilized discrete wavelet transform to extracmultiresolution features from current vectors in the harmonic plane, subsequently performing fault diagnosis based on SVM after dimensionality reduction. This strategy primarily addresses OPF, but it still encounters numerous misdiagnosis cases for this easily distinguishable fault type, with offline diagnosis accuracy limited to 96.40%. Yao et al. [43] employed EMD and HT for fault detection in five-phase PMSM drive systems. This method identifies and locates fault types using a variable parameter PSO algorithm. However, it is restricted to OPF and is unsuitable for switch faults. Additionally, it does not adequately address robustness under load variations. Chahba et al. [35] applied an MLP neural network combined with a FFT-based feature extractor to detect OPF in five-phase IM, achieving an offline diagnosis accuracy of 97.40%. However, the online diagnosis time exceeds 1.5 FP, leading to longer diagnosis durations.

In contrast, the fault diagnosis strategy proposed in this paper achieves an impressive offline accuracy of 99.58% using only simulation domain data, thereby eliminating the need for precollected experimental domain data.. The online diagnosis

time requires merely 0.9 FP, even under worst-case conditions, demonstrating exceptional computational efficiency and accuracy. Furthermore, this strategy remains unaffected by operating conditions such as rotor speed and load torque, showcasing resilience against nonideal factors like current ripples and electromagnetic noise. Importantly, It is applicable to multiphase motor drive systems with varying parameters and types, exhibiting remarkable generalization capabilities.

IV. Conclusion

To address the challenge of limited experimental domain data in open-circuit fault diagnosis of multiphase converters, this article presents an innovative domain generalization model. The model only requires training on simulated domain samples to effectively tackle fault diagnosis tasks within the experimental domain. The core innovations of this study are as follows.

1) A normalization preprocessing technique based on phase current reconstruction is proposed. This technique reduces temporal discrepancies in phase current data between the simulation and experimental domains, thus providing a robust foundation for high-quality feature extraction and significantly enhances the model's discriminative ability. As a result, the adaptability of models trained on simulation domain data is greatly improved when applied to experimental domain data.
2) Recognizing that generalization model employing traditional network architecture may not achieve satisfactory diagnostic performance in practical applications, we have developed a convolutional auto-encoder network integrated with deep metric learning. This network enhances the model's ability to process features of different subclasses by optimizing the degree of within-class compactness, thereby increasing the model's clustering potential. This structural design allows the model to improve diagnostic accuracy, precision, and recall, while also demonstrating strong generalization performance.

This article effectively bridges the gap between numerical simulation and actual fault diagnosis, significantly enhancing the accuracy and precision of intelligent diagnostic models in practical applications.

References

[1] G. Yang, H. Hussain, S. Li, J. Zhang, and J. Yang, "A unified fault-tolerant strategy for multiphase machine with minimum losses in full torque operation range based on closed-form expressions," *IEEE Trans. Power Electron.*, vol. 37, no. 10, pp. 12463–12473, Oct. 2022.

[2] C. Zhang et al., "Compatible phase current reconstruction scheme for fault-tolerant five-leg dual-inverter fed open-winding permanent magnet synchronous motor," *IEEE Trans. Power Electron.*, vol. 38, no. 8, pp. 10073–10084, Aug. 2023.

[3] J. Sun, Z. Liu, Z. Zheng, and Y. Li, "An online global fault-tolerant control strategy for symmetrical multiphase machines with minimum losses in full torque production range," *IEEE Trans. Power Electron.*, vol. 35, no. 3, pp. 2819–2830, Mar. 2020.

[4] Z. Gao, C. Cecati, and S. X. Ding, "A survey of fault diagnosis and fault-tolerant techniques—Part II: Fault diagnosis with knowledge-based and hybrid/active approaches," *IEEE Trans. Ind. Electron.*, vol. 62, no. 6, pp. 3768–3774, Jun. 2015.

[5] S. Zhuo, A. Gaillard, L. Xu, C. Liu, D. Paire, and F. Gao, "An observer-based switch open-circuit fault diagnosis of DC–DC converter for fuel cell application," *IEEE Trans. Ind. Appl.*, vol. 56, no. 3, pp. 3159–3167, May/Jun. 2020.

[6] D. Xie and X. Ge, "A State estimator-based approach for open-circuit fault diagnosis in single-phase cascaded H-bridge rectifiers," *IEEE Trans. Ind. Appl.*, vol. 55, no. 2, pp. 1608–1618, Mar./Apr. 2019.

[7] D. Zhou, S. Yang, and Y. Tang, "A voltage-based open-circuit fault detection and isolation approach for modular multilevel converters with model-predictive control," *IEEE Trans. Power Electron.*, vol. 33, no. 11, pp. 9866–9874, Nov. 2018.

[8] W. Huang et al., "Current-based open-circuit fault diagnosis for PMSM drives with model predictive control," *IEEE Trans. Power Electron.*, vol. 36, no. 9, pp. 10695–10704, Sep. 2021.

[9] Y. Wang, X. Xu, C. Qiu, Z. Zheng, K. Wang, and Y. Li, "A data-driven open-circuit fault diagnosis method for three-phase T-type three-level inverters," in *Proc. IEEE Int. Power Electron. Application Conf. Expo.*, 2022, pp. 95–100.

[10] J. Hang, X. Shu, S. Ding, and Y. Huang, "Robust open-circuit fault diagnosis for PMSM drives using wavelet convolutional neural network with small samples of normalized current vector trajectory graph," *IEEE Trans. Ind. Electron.*, vol. 70, no. 8, pp. 7653–7663, Aug. 2023.

[11] H. Zhang, X. Guo, and P. Zhang, "Improved PSO-SVM-based fault diagnosis algorithm for wind power converter," in *Proc. 4th Int. Conf. Smart Power Internet Energy Syst.*, 2022, pp. 1213–1216.

[12] B. Gou, Y. Xu, Y. Xia, Q. Deng, and X. Ge, "An online data-driven method for simultaneous diagnosis of IGBT and current sensor fault of three-phase PWM inverter in induction motor drives," *IEEE Trans. Power Electron.*, vol. 35, no. 12, pp. 13281–13294, Dec. 2020.

[13] Z. Li, Y. Gao, X. Zhang, B. Wang, and H. Ma, "A model-data-hybrid-driven diagnosis method for open-switch faults in power converters," *IEEE Trans. Power Electron.*, vol. 36, no. 5, pp. 4965–4970, May 2021.

[14] C. Liu and K. Gryllias, "Simulation-driven domain adaptation for rolling element bearing fault diagnosis," *IEEE Trans. Ind. Informat.*, vol. 18, no. 9, pp. 5760–5770, Sep. 2022.

[15] B. Gou, Y. Xu, Y. Xia, G. Wilson, and S. Liu, "An intelligent time-adaptive data-driven method for sensor fault diagnosis in induction motor drive system," *IEEE Trans. Ind. Electron.*, vol. 66, no. 12, pp. 9817–9827, Dec. 2019.

[16] B. Cai, Y. Zhao, H. Liu, and M. Xie, "A data-driven fault diagnosis methodology in three-phase inverters for PMSM drive systems," *IEEE Trans. Power Electron.*, vol. 32, no. 7, pp. 5590–5600, Jul. 2017.

[17] T. Han, Y.-F. Li, and M. Qian, "A hybrid generalization network for intelligent fault diagnosis of rotating machinery under unseen working conditions," *IEEE Trans. Instrum. Meas.*, vol. 70, 2021, Art. no. 3520011.

[18] U. Mupambireyi, L. Ran, A. Crane, and P. Mawby, "A multiphase machine and converter topology for renewable energy generation," in *Proc. IEEE Energy Convers. Congr. Expo.*, 2018, pp. 304–311.

[19] C. Onambele, A. Mpanda, M. Elsied, and F. Giacchetti, "Co-simulation modeling of high performance motor-drive systems for aerospace applications," in *Proc. IEEE Int. Elect. Mach. Drives Conf.*, 2017, pp. 1–6.

[20] J. Gong et al., "Design, Analysis of a seven-phase fault-tolerant Biharmonic permanent magnet machine with three active air gaps for In-wheel traction applications," *IEEE Trans. Energy Convers.*, vol. 39, no. 1, pp. 263–276, Mar. 2024.

[21] Y. Xia and Y. Xu, "A transferrable data-driven method for IGBT open-circuit fault diagnosis in three-phase inverters," *IEEE Trans. Power Electron.*, vol. 36, no. 12, pp. 13478–13488, Dec. 2021.

[22] D. U. Campos-Delgado, J. A. Pecina-Sánchez, D. R. Espinoza-Trejo, and E. R. Arce-Santana, "Diagnosis of open-switch faults in variable speed drives by stator current analysis and pattern recognition," *Inst. Eng. Technol. Elect. Power Appl.*, vol. 7, no. 6, pp. 509–522, Jul. 2013.

[23] A. Tani, M. Mengoni, L. Zarri, G. Serra, and D. Casadei, "Control of multiphase induction motors with an odd number of phases under open-circuit phase faults," *IEEE Trans. Power Electron.*, vol. 27, no. 2, pp. 565–577, Feb. 2012.

[24] I. G. Prieto, M. J. Duran, P. Garcia-Entrambasaguas, and M. Bermudez, "Field-oriented control of multiphase drives with passive fault tolerance," *IEEE Trans. Ind. Electron.*, vol. 67, no. 9, pp. 7228–7238, Sep. 2020.

[25] M. Trabelsi, E. Semail, and N. K. Nguyen, "Experimental investigation of inverter open-circuit fault diagnosis for biharmonic five-phase permanent magnet drive," *IEEE J. Emerg. Sel. Topics Power Electron.*, vol. 6, no. 1, pp. 339–351, Mar. 2018.

[26] Z. Zhang, Y. Hu, G. Luo, H. Xu, and C. Gong, "Analysis and real-time calculation of postfault current of standard surface-mounted PMSM drives with dysfunctional power switches," *IEEE Trans. Power Electron.*, vol. 38, no. 8, pp. 10104–10115, Aug. 2023.

[27] Z. Liu, L. Fang, D. Jiang, and R. Qu, "A machine-learning-based fault diagnosis method with adaptive secondary sampling for multiphase drive systems," *IEEE Trans. Power Electron.*, vol. 37, no. 8, pp. 8767–8772, Aug. 2022.
[28] Y. Du, C. Li, and Z. Zheng, "Current sensor fault diagnosis of MUPMSM drive system using similarity learning," in *Proc. IEEE Veh. Power Propulsion Conf.*, 2023, pp. 1–8.
[29] J. O. Estima, N. M. A. Freire, and A. J. M. Cardoso, "Recent advances in fault diagnosis by Park's vector approach," in *Proc. IEEE Workshop Elect. Machines Des., Control Diagnosis*, 2013, pp. 279–288.
[30] N. M. A. Freire, J. O. Estima, and A. J. M. Cardoso, "A new approach for current sensor fault diagnosis in PMSG drives for wind energy conversion systems," *IEEE Trans. Ind. Appl.*, vol. 50, no. 2, pp. 1206–1214, Mar./Apr. 2014.
[31] H. Wang, J. Xu, R. Yan, and R. X. Gao, "A new intelligent bearing fault diagnosis method using SDP representation and SE-CNN," *IEEE Trans. Instrum. Meas.*, vol. 69, no. 5, pp. 2377–2389, May 2020.
[32] D. Zhang, Y. Chen, F. Guo, H. R. Karimi, H. Dong, and Q. Xuan, "A new interpretable learning method for fault diagnosis of rolling bearings," *IEEE Trans. Instrum. Meas.*, vol. 70, 2021, Art. no. 3507010.
[33] S. Yan, X. Zhong, H. Shao, Y. Ming, C. Liu, and B. Liu, "Digital twin-assisted imbalanced fault diagnosis framework using subdomain adaptive mechanism and margin-aware regularization," *Reliab. Eng. Syst. Saf.*, vol. 239, 2023, Art. no. 109522.
[34] X. Hu, H. Jia, Y. Zhang, and Y. Deng, "An open-circuit faults diagnosis method for MMC based on extreme gradient boosting," *IEEE Trans. Ind. Electron.*, vol. 70, no. 6, pp. 6239–6249, Jun. 2023.
[35] S. Chahba, R. Sehab, A. Akrad, and C. Morel, "A neural network approach for an automatic detection and localization of an open phase circuit of a five-phase induction machine used in a drivetrain of an electric vehicle," in *Proc. Int. Conf. Control, Automat. Diagnosis*, 2022, pp. 1–8.
[36] Z. Li, H. Ma, Z. Bai, Y. Wang, and B. Wang, "Fast transistor open-circuit faults diagnosis in grid-tied three-phase VSIs based on average bridge arm pole-to-pole voltages and error-adaptive thresholds," *IEEE Trans. Power Electron.*, vol. 33, no. 9, pp. 8040–8051, Sep. 2018.
[37] Z. Peng, Z. Zheng, Y. Li, and Z. Liu, "Sensorless vector control of multiphase induction machine based on full-order observer and harmonic suppression," in *Proc. IEEE 3rd Int. Future Energy Electron. Conf. ECCE Asia*, 2017, pp. 2153–2160.
[38] Y. Ma, D. Jiang, Z. Liu, S. Yan, Z. Wang, and R. Qu, "Common-mode voltage elimination of dual three-phase motor with different angular displacements," *IEEE Trans. Ind. Electron.*, vol. 71, no. 6, pp. 5431–5442, Jun. 2024.
[39] C. Olivieri, "A fault-adaptive and observer-based sensorless strategy for a fault-tolerant five-phase BLDC motor," in *Proc. IEEE Int. Symp. Sensorless Control Elect. Drives Predictive Control Elect. Drives Power Electron.*, 2013, pp. 1–8.
[40] N. Torabi, V. M. Sundaram, and H. A. Toliyat, "On-line fault diagnosis of multi-phase drives using self-recurrent wavelet neural networks with adaptive learning rates," in *Proc. IEEE Appl. Power Electron. Conf. Expo.*, 2017, pp. 570–577.
[41] Z. Huang, Z. Wang, and L. Liu, "A practical fault diagnosis algorithm based on aperiodic corrected-second low-frequency processing for microgrid inverter," *IEEE Trans. Ind. Informat.*, vol. 15, no. 7, pp. 3889–3898, Jul. 2019.
[42] M. Shao, G. Yang, G. Sun, and J. Su, "A method of open circuit fault diagnosis for five-phase permanent magnet synchronous motor based on wavelet analysis," in *Proc. 22nd Int. Conf. Elect. Mach. Syst.*, 2019, pp. 1–6.
[43] G. Yao, S. Pang, T. Ying, M. Benbouzid, M. Ait-Ahmed, and M. F. Benkhoris, "VPSO-SVM-based open-circuit faults diagnosis of five-phase marine current generator sets," *Energies*, vol. 13, 2020, Art. no. 6004.

Haoxiang Xu (Student Member, IEEE) was born in Liaoning, China, in 2001. He received the B.S. degree in electrical engineering from Nanchang University, Nanchang, China, in 2023. He is currently working toward the Ph.D. degree in electrical engineering in the School of Electronic and Electrical Engineering, Huazhong University of Science and Technology, Wuhan, China.

His current research interests include intelligent condition monitoring, and fault prediction and diagnosis technology of motor drive system.

Zicheng Liu (Senior Member, IEEE) received the B.S. degree in hydropower engineering from the Huazhong University of Science and Technology (HUST), Wuhan, China, in 2011, and the Ph.D. degree in electrical engineering from Tsinghua University, Beijing, China, in 2016.

From 2014 to 2015, he was a Visiting Student with Purdue University, West Lafayette, IN, USA. During 2016 to 2018, he was a Postdoc Researcher with Beijing Jiaotong University, Beijing, China. He is currently an Associate Professor with HUST. His research interests include multiphase motor control systems and transportation electrification.

Dr. Liu was the recipient of the best letter award of IEEE TRANSACTIONS ON POWER ELECTRONICS, the second-place prize paper award of IEEE JOURNAL OF EMERGING AND SELECTED TOPICS IN POWER ELECTRONICS, and three prize paper awards in IEEE conferences. He is the Vice Chair of IEEE Power Electronics Society Wuhan Chapter.

Guangyu Wang (Student Member, IEEE) was born in Jiangxi, China, in 2001. He received the B.S. degree in electrical engineering from Dalian Maritime University, Liaoning, China, in 2023. He is currently working toward the Ph.D. degree in electrical engineering in the School of Electronic and Electrical Engineering, Huazhong University of Science and Technology, Wuhan, China.

His current research interests include multiphase motor control and fault-tolerant control.

Dong Jiang (Senior Member, IEEE) received the B.S. and M.S. degrees in electrical engineering from Tsinghua University, Beijing, China, in 2005 and 2007, respectively, and the Ph.D. degree in power electronics and motor drives from the University of Tennessee, Knoxville, TN, USA, in 2011.

He was with the United Technologies Research Center, East Hartford, CT, USA, as a Senior Research Scientist/Engineer, from 2012 to 2015. He has been with the Huazhong University of Science and Technology, Wuhan, China, as a Professor, since 2015. His main research interests include power electronics and motor drives, with more than 100 published IEEE journal and conference papers and more than 40 granted patents in this area.

Dr. Jiang is an Associate Editor for IEEE TRANSACTIONS ON INDUSTRY APPLICATIONS. He was the recipient of several best paper awards in IEEE conferences.

Wei Sun (Member, IEEE) received the B.S. degree from Beijing Jiaotong University, Beijing, China, in 2009, and the M.S. and Ph.D. degrees from the Harbin Institute of Technology, Harbin, China, in 2012 and 2016, respectively, all in electrical engineering.

He has been with the Huazhong University of Science and Technology, Wuhan, China, as an Assistant Professor, since 2017. His research interests include ac motor drive, and control theory application in power electronics system.